

1 **Mechanics-based optimization of yolk-shell carbon-coated**
2 **silicon nanoparticle as electrode materials for high-capacity**
3 **lithium ion battery**

4 Weiqun Li^{a,†}, Qian Wang^{a,†}, Ke Cao^b, Jingjing Tang^a, Hongtao Wang^c, Limin Zhou^{a,*},
5 Haimin Yao^{a,*}

6 ^a Department of Mechanical Engineering, The Hong Kong Polytechnic University, Hung
7 Hom, Kowloon, Hong Kong, P. R. China

8 ^b School of Materials Science and Engineering, Zhejiang University, Hangzhou 310027,
9 P. R. China

10 ^c Institute of Applied Mechanics, Zhejiang University, Hangzhou 310027, P. R. China

11

12 **Abstract**

13 Yolk-shell carbon-coated silicon nanoparticles (Si@void@C NPs) have been
14 demonstrated to have a great promise in solving the problem of significant volume
15 change of silicon-based anode materials during lithiation and delithiation cycling.
16 However, our *in situ* lithiation experiments show that Si@void@C NPs may still subject
17 to fracture upon lithiation, depending on their characteristic structural features such as the
18 size of Si yolk, the thickness of carbon shell, and the interspace between the yolk and
19 shell. Given the size of Si yolk, to ensure structural integrity of Si@void@C NPs during
20 lithiation and delithiation, thicker carbon shell and larger yolk-shell interspace are
21 preferred. On the other hand, from the perspective of attaining higher effective capacity,
22 thinner carbon shell and smaller yolk-shell interspace are favored. To find the optimal
23 structural design which yields the maximum capacity and meanwhile ensure the integrity

* Corresponding authors. mmhyao@polyu.edu.hk (H. Yao); E-mail: mmlmzhou@polyu.edu.hk (L. Zhou).

† These authors contributed equally to this work.

24 of Si@void@C NPs during lithiation, mechanics-based theoretical modeling is carried
25 out. A diagram for structural optimizations is obtained, by which the optimized
26 Si@void@C NPs are synthesized and found to have improved capacity and capacity
27 retention compared to the unoptimized ones. The results of this paper provide a guideline
28 for the design of Si@void@C NPs as anode materials for high-capacity lithium ion
29 battery.

30

31 **Keywords**

32 Anode, *in situ* TEM, fracture mechanics, optimal design

33

34 **1. Introduction**

35 Lithium ion battery (LIB), as an energy storage and supply unit, has been widely used
36 in various devices from household electrics to industrial facilities [1]. In order to achieve
37 high capacity and long lifespan, a variety of electrode materials of LIB have been applied.
38 The prevailing carbon-based anode materials, despite of long cycle life, exhibit low
39 capacity ($372 \text{ mA h}\cdot\text{g}^{-1}$) [2,3]. In contrast, silicon (Si) anode materials possess high
40 capacity ($4200 \text{ mA h}\cdot\text{g}^{-1}$) but suffer from fracture and pulverization due to the large
41 volume change ($\sim 400\%$) during lithiation and delithiation cycling, leading to poor cycle
42 life [4]. Although reducing the Si anode materials to nanoscale has been demonstrated to
43 have improved performance, solid electrolyte interface (SEI) would form on their
44 surfaces whose repeated fracture and thickening, upon cyclic lithiation and delithiation,
45 consume the Si and electrolyte, leading to the degradation of electrochemical
46 performance of the battery [5-7]. To solve this problem, carbon-coated Si nanowires and
47 nanoparticles (NPs) have been developed and found able to improve the cycle life of pure

48 nano Si materials [8-10]. However, because of the adding of carbon whose specific
49 capacity is much lower compared to that of Si, the effective capacity of the anode
50 material decreases. Structural optimization was applied to maximize the capacity on the
51 condition that the structural integrity got ensured [11,12]. More recently, yolk-shell
52 carbon-coated Si (Si@void@C) NPs, which incorporate spare space between the Si yolk
53 and carbon shell, have been developed, exhibiting much better electrochemical
54 performance [13-20]. The improved cycling performance is mainly due to the interspace
55 that can accommodate the lithiation-induced expansion of the Si yolk and thereby
56 mitigates the stress and deformation of the carbon shell. As a consequence, the SEI
57 formed on the surface of carbon shell will not fracture during the electrochemical cycling.
58 Nevertheless, in literature the capacities of the LIBs using Si@void@C NPs as anode
59 materials exhibit a wide spectrum ranging from a few hundreds to more than 2000 mA
60 $\text{h}\cdot\text{g}^{-1}$, implying much room in optimizing the Si@void@C NPs. For example, it is still
61 unclear how much space should be spared between the Si yolk and carbon shell and how
62 thick the carbon shell should be so as to achieve the highest capacity and simultaneously
63 maintain the structural integrity of Si@void@C NPs during lithiation and delithiation
64 cycling. The objective of this paper is to find such optimal design of Si@void@C NP, at
65 least in principle, for high-capacity LIBs.

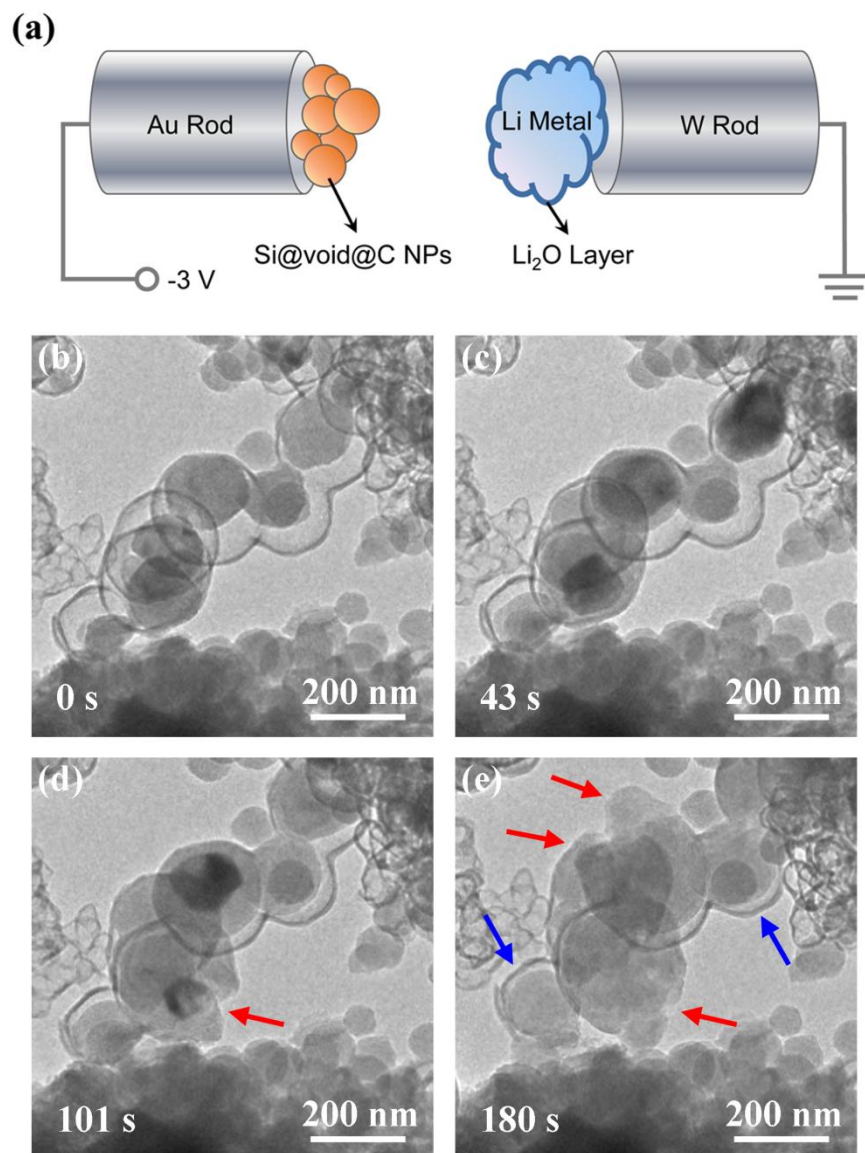
66 The remaining of this paper proceeds as follows. First, we carry out *in situ* lithiation
67 on individual Si@void@C NPs with different sizes and shell thicknesses to deduce the
68 factors determining the failure of Si@void@C NPs during lithiation. Then, a rigorous
69 theoretical model is established to formulate the dependence of structural integrity of
70 Si@void@C NP during lithiation on its structural attributes such as the shell thickness,

71 yolk size and yolk-shell interspace. Then, the theoretical effective capacity of
72 Si@void@C NP is estimated simply by combining the fractional contributions from the
73 carbon and Si compositions. By considering the requirements from structural integrity
74 and effective capacity together, a diagram of structural optimization is proposed and used
75 to guide the synthesis of the optimized Si@void@C NPs. Using the optimized
76 Si@void@C NPs as the anode material, coin-type half-cells are prepared and the
77 electrochemical performance is characterized. The whole paper is concluded by
78 analyzing the results and discussing the limitation of the present work.

79 **2. Results**

80 **2.1. *In situ* lithiation of individual yolk-shell carbon-coated silicon nanoparticles**

81 The Si@void@C NPs were synthesized by using Stöber method [13,21,22] and the *in*
82 *situ* lithiation of the NPs is carried out inside TEM by using a nanoscale battery setup as
83 shown in Fig. 1a (See Supplementary Material for details). The morphologies of the
84 pristine Si@void@C NPs are shown in Fig. 1b. After 43 s of lithiation, the Si yolks are
85 found to be lithiated partially as seen from their volume expansion and the clear interface
86 between the lithiated and unlithiated Si (Fig. 1c). As the Si yolk swells, the gap between
87 the yolk and shell becomes smaller and smaller. It can be seen from Fig. 1d that one of
88 the NPs (indicated by red arrow) has been fractured at 101 s. Fig. 1e shows the
89 morphologies at full lithiation, when more NPs (indicated by red arrows) are fractured
90 while some NPs (indicated by blue arrows) remain continuous.

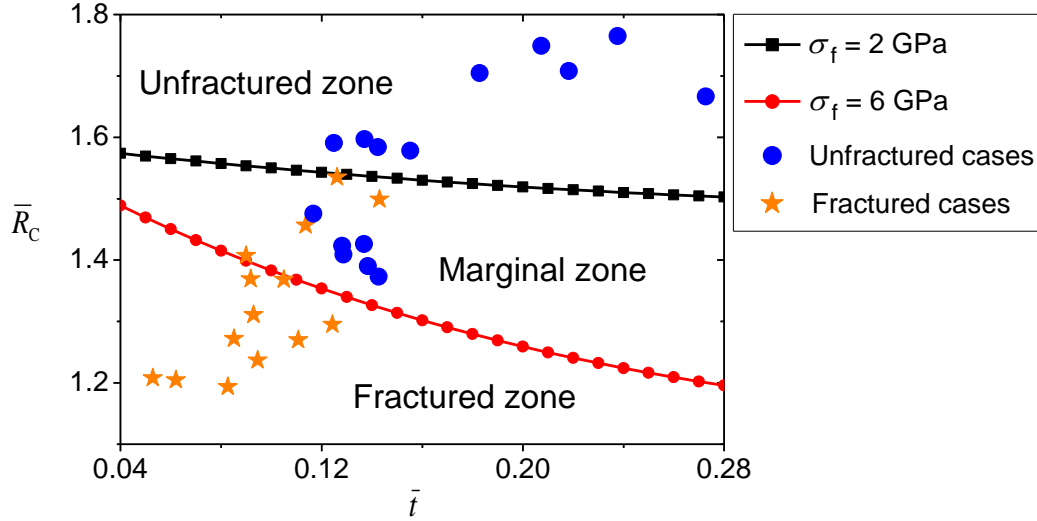


91

92 Figure 1. (a) Schematic of the setup for *in situ* lithiation. (b-e) Snapshots of the lithiation
 93 process for the Si@void@C NPs.

94 The above *in situ* lithiation is repeated on dozens of Si@void@C NPs and the
 95 consequences of lithiation (fractured versus unfractured) are displayed on the $\bar{R}_C - \bar{t}$ plane,
 96 as shown in Fig. 2. Here \bar{R}_C and \bar{t} are the radius of carbon shell R_C and the thickness of
 97 carbon shell t normalized by the radius of Si yolk R_{Si} . It can be seen that the

98 Si@void@C NPs tend to be fractured with lower \bar{R}_C and \bar{t} while remain continuous if
 99 \bar{R}_C and \bar{t} are higher, indicating clear dimension-dependent fracture of Si@void@C NPs
 100 upon lithiation.



101
 102 Figure 2. Dimension-dependent fracture of Si@void@C NPs.

103 2.2. Theoretical modeling of structural integrity

104 In order to account for the dimension-dependent fracture of the Si@void@C NPs
 105 observed during *in situ* lithiation, the stress in the carbon shell caused by lithiation-
 106 induced expansion of the Si yolk is examined by theoretical modeling based on the theory
 107 of elasticity [23] (see Supplementary Material for details). The analytical solution to the
 108 maximum tensile stress σ_t^{\max} in the carbon shell is given by

$$\begin{aligned}
 \sigma_t^{\max} = E_C(1 + \varepsilon_0 - \bar{R}_C + 0.5\bar{t}) & \left\{ \frac{3\bar{R}_C^2\bar{t} + 0.25\bar{t}^3}{3\bar{R}_C^3 - 1.5\bar{R}_C^2\bar{t} + 2.25\bar{R}_C\bar{t}^2 - 0.125\bar{t}^3} \right. \\
 & \times \left[2\nu_C(\bar{R}_C - 0.5\bar{t}) + \frac{2E_C}{E_{\text{Li,Si}}}(1 - 2\nu_{\text{Li,Si}})(\bar{R}_C - 0.5\bar{t})^2 \right] + (1 - \nu_C)(\bar{R}_C - 0.5\bar{t}) \left. \right\} \quad (1)
 \end{aligned}$$

110 where ε_0 is the linear expansion ratio of a free Si NP at full lithiation. In this paper, we
111 take $\varepsilon_0 = 0.6$ corresponding to volume expansion of $\sim 400\%$ [24]. Additionally, both
112 lithiated Si and amorphous carbon are assumed as elastic with Young's moduli and
113 Poisson's ratios being $E_{\text{Li}_x\text{Si}} = 3.5 \text{ GPa}$ [25], $\nu_{\text{Li}_x\text{Si}} = 0.23$ [26] and $E_{\text{C}} = 300 \text{ GPa}$,
114 $\nu_{\text{C}} = 0.25$ [27], respectively. For lithiated Si which possesses large ductility, such elastic
115 assumption is also reasonable because the stress state in the yolk is hydrostatic
116 compression which causes no plastic deformation.

117 According to the maximum tensile stress criterion [28], the carbon shell will fracture
118 if the maximum tensile stress, σ_t^{max} , exceeds the fracture strength, σ_f , of the material.
119 By equating the σ_t^{max} in Eq. (1) with the fracture strength of amorphous carbon, the
120 critical condition for the fracture can be determined in terms of \bar{R}_{C} and \bar{t} . Taking the
121 fracture strength of amorphous carbon as 2 GPa and 6 GPa respectively, the critical
122 condition for fracture is plotted as two curves on the $\bar{R}_{\text{C}} - \bar{t}$ plane (Fig. 2). If the structural
123 features of NPs, characterized by \bar{R}_{C} and \bar{t} , fall in the region below the critical curve, the
124 carbon shell will be cracked. Otherwise, it remains continuous. Comparing the
125 experimental observations (the scattering symbols in Fig. 2) and the theoretical prediction
126 (the solid curves in Fig. 2), we can see that all the fractured cases are below the curve of
127 $\sigma_f = 6 \text{ GPa}$ while all the unfractured cases are above the curve corresponding to $\sigma_f = 2$
128 GPa, implying that the fracture strength of the carbon coating in our samples is not
129 uniform but in the range from 2 to 6 GPa. This agrees well with the spectrum of the
130 fracture strength of amorphous carbon as reported in literature [29]. As a conservative

131 design ensuring structural integrity, the dimensions of Si@void@C NPs (\bar{R}_C and \bar{t})
 132 should fall in the region above the critical curve corresponding to $\sigma_f = 2$ GPa in Fig. 2.

133 2.3. Capacity optimization and experimental verification

134 Besides the structural integrity of the Si@void@C NPs, it is also important to attain
 135 high capacity of the Si@void@C NPs. The theoretical capacity of the Si@void@C NPs
 136 can be estimated from the theoretical capacities, mass fractions, and volume expansion of
 137 the Si and carbon compositions. Assuming that for unfractured Si@void@C NPs the
 138 amount of inserted Li^+ in Si yolk is proportional to its volume change and carbon shell is
 139 fully lithiated, the theoretical capacity of the Si@void@C NP can be expressed as (see
 140 Supplementary Material for detailed derivation)

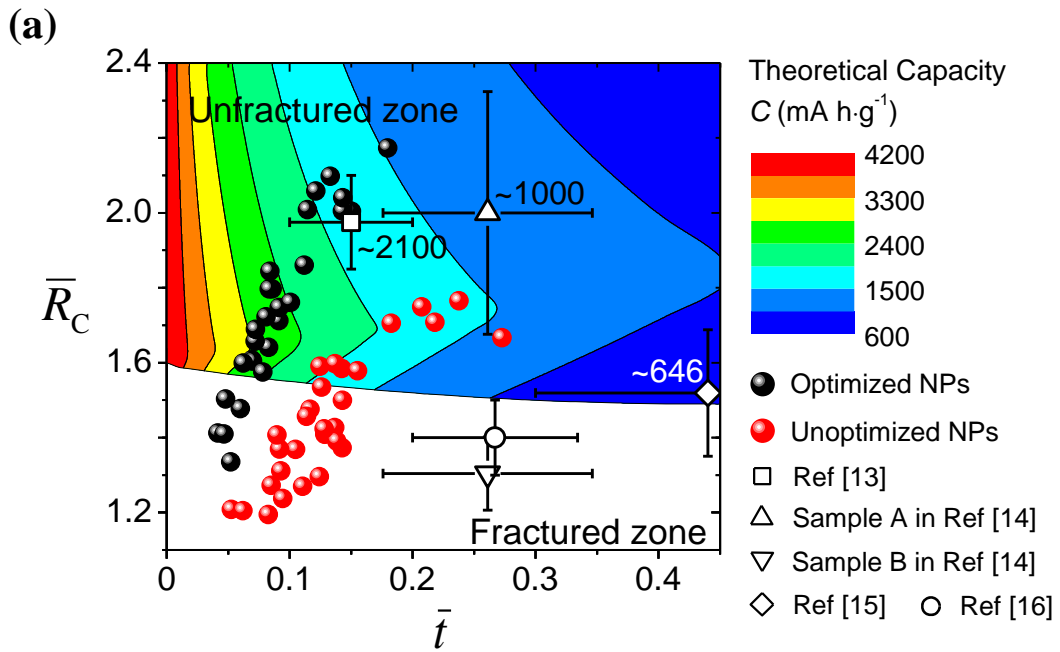
$$141 \quad C = \frac{C_{\text{Si}}}{1 + \bar{\rho}(3\bar{R}_C^2\bar{t} + 0.25\bar{t}^3)} \frac{(1 + \varepsilon_0 - \varepsilon_{\text{Si}})^3 - 1}{(1 + \varepsilon_0)^3 - 1} + \frac{C_C \bar{\rho}(3\bar{R}_C^2\bar{t} + 0.25\bar{t}^3)}{1 + \bar{\rho}(3\bar{R}_C^2\bar{t} + 0.25\bar{t}^3)} \quad (2)$$

142 with

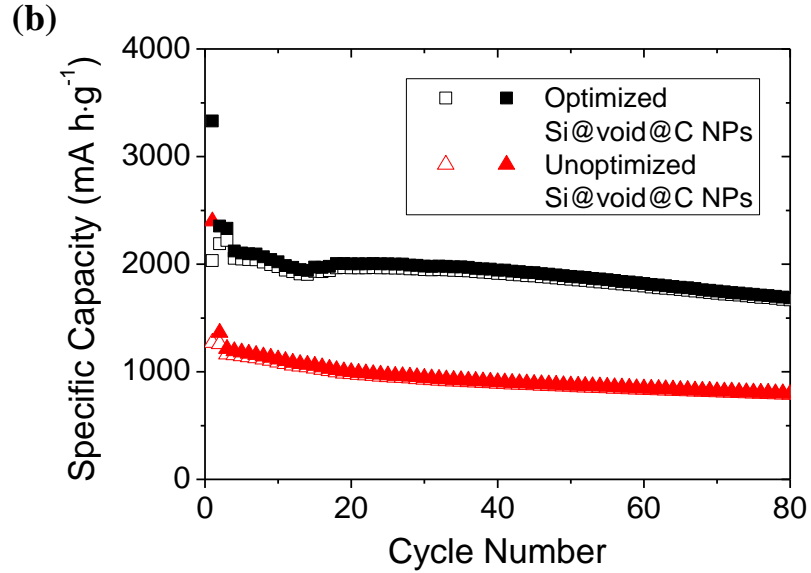
$$143 \quad \varepsilon_{\text{Si}} = 2(1 - 2\nu_{\text{Li,Si}})(1 + \varepsilon_0 - \bar{R}_C + 0.5\bar{t})(\bar{R}_C - 0.5\bar{t})^2 / \left[\frac{2E_{\text{Li,Si}}\nu_C}{E_C}(\bar{R}_C - 0.5\bar{t}) + 2(1 - 2\nu_{\text{Li,Si}}) \times \right. \\ \left. (\bar{R}_C - 0.5\bar{t})^2 + \frac{E_{\text{Li,Si}}}{E_C}(1 - \nu_C)(\bar{R}_C - 0.5\bar{t}) \frac{3\bar{R}_C^3 - 1.5\bar{R}_C^2\bar{t} + 2.25\bar{R}_C\bar{t}^2 - 0.125\bar{t}^3}{3\bar{R}_C^2\bar{t} + 0.25\bar{t}^3} \right]$$

144 In above expressions, C_{Si} and C_C are the theoretical capacities of Si and carbon [24], $\bar{\rho}$
 145 denotes the density ratio between carbon and Si, and ε_{Si} is the radial strain of the fully
 146 lithiated Si yolk under the constraint of the carbon shell. Taking the typical values of
 147 $C_{\text{Si}} = 4200 \text{ mA h} \cdot \text{g}^{-1}$, $C_C = 372 \text{ mA h} \cdot \text{g}^{-1}$, $\bar{\rho} = 0.966$ [24], $E_{\text{Li,Si}} = 3.5 \text{ GPa}$ [25],

148 $\nu_{\text{Li,Si}} = 0.23$ [26] and $E_C = 300$ GPa, $\nu_C = 0.25$ [27], $\varepsilon_0 = 0.6$, the capacity C given in
 149 Eq. (2), as a function of \bar{R}_C and \bar{t} , is shown by the contours on the $\bar{R}_C - \bar{t}$ plane, as in Fig.
 150 3a. Here, only the unfractured zone corresponding to $\sigma_f = 2$ GPa is considered due to
 151 the unpredictability of the capacity of the fractured Si@void@C NPs.



152



153

154 Figure 3. (a) Dependence of the predicted capacity of the unfractured Si@void@C NPs
 155 on \bar{R}_c and \bar{t} . The black and red solid spheres represent the distributions of the
 156 dimensions of the optimized and unoptimized Si@void@C NPs respectively, while the
 157 hollow symbols represent the dimensions ranges of the Si@void@C NPs in the
 158 literatures. Here, samples A and B correspond to the “YS Si@50mC” and “YS Si@10mC”
 159 in Ref. [14] respectively. (b) Lithiation (solid symbols) and delithiation (hollow symbols)
 160 capacities for galvanostatic cycles of the optimized and unoptimized Si@void@C NPs.
 161 The current density is $200 \text{ mA}\cdot\text{g}^{-1}$ for the first two cycles while $500 \text{ mA}\cdot\text{g}^{-1}$ for the later
 162 cycles which is close to that taken in Ref. [13-16].

163 Fig. 3a provides the guideline for gaining higher capacity by optimizing the
 164 dimensions of Si@void@C NPs. Under the direction of Fig. 3a, a new batch of
 165 Si@void@C NPs are synthesized. The dimensions (\bar{R}_c and \bar{t}) of some representative
 166 optimized NPs are shown by the black spheres in Fig. 3a, in comparison to those of the
 167 unoptimized ones (denoted by the red spheres) used in the *in situ* lithiation above. It can
 168 be seen that most of the optimized Si@void@C NPs possess dimensions falling in the
 169 unfractured zone (corresponding to $\sigma_f = 2 \text{ GPa}$). The averaged capacity of the optimized

170 NPs, as estimated on the basis of Eq. (2), is around $2250 \text{ mA h}\cdot\text{g}^{-1}$. To verify such
171 theoretical predictions, electrochemical cycling measurement is conducted by using the
172 as-fabricated optimized NPs as the anode materials (See Supplementary Material for
173 details). The results are shown in Fig. 3b in comparison to those of the control case using
174 the unoptimized Si@void@C NPs. Clearly, the galvanostatic cycling performance of the
175 optimized Si@void@C NPs is more stable than that of the unoptimized one. The
176 unoptimized NPs exhibit 67.8% capacity retention with reversible capacity of 787.6 mA
177 $\text{h}\cdot\text{g}^{-1}$ after 80 cycles, while the optimized NPs achieve capacity retention of 75.1% and
178 reversible capacity of $1666.9 \text{ mA h}\cdot\text{g}^{-1}$ after 80 cycles. Clear improvement of the
179 electrochemical cycling performance is observed by dimensional optimization of the
180 Si@void@C NPs.

181 In literature, similar Si@void@C NPs with various dimensions have also been
182 produced using different protocols. It might be also interesting to use our theory to make
183 an estimation of the capacities of these Si@void@C NPs and then make a comparison
184 with their measured values. The hollow symbols with error bars in Fig. 3a show the
185 ranges of the dimensions of the Si@void@C NPs reported in Ref. [13-16]. Among them,
186 three groups of Si@void@C NPs have dimensions distributed in the “unfractured” zone.
187 According to Eq. (2), their capacities are estimated to be $1546\text{-}2169 \text{ mA h}\cdot\text{g}^{-1}$, $1135\text{-}1631$
188 $\text{mA h}\cdot\text{g}^{-1}$ and $535\text{-}972 \text{ mA h}\cdot\text{g}^{-1}$, agreeing well with their measured values $\sim 2100 \text{ mA}$
189 $\text{h}\cdot\text{g}^{-1}$, $\sim 1000 \text{ mA h}\cdot\text{g}^{-1}$ and $\sim 646 \text{ mA h}\cdot\text{g}^{-1}$, respectively. For the other two groups, our
190 theory indicates that they will be fractured during lithiation. This prediction may explain
191 why the capacities of these samples drop quickly with cycling.

192

193 **3. Discussion and conclusion**

194 For our optimized Si@void@C NPs, the capacity we obtained above is 1666.9 mA
195 h·g⁻¹, which is lower than the theoretical estimation of ~2250 mA h·g⁻¹. This might be
196 due to the capacity loss after first delithiation, which results from the formation of SEI
197 and the irreversible alloying of Li⁺ with Si and carbon [13,30]. Besides, the dimensions
198 of our Si@void@C NPs are not uniform. There are still some NPs in our optimized
199 sample being fractured during lithiation and delithiation, resulting in the decrease of
200 capacity [31]. For higher capacity, further optimization of the dimensions of the NPs is
201 needed.

202 In conclusion, in this communication, *in situ* lithiation on the synthesized
203 Si@void@C NPs is conducted, showing the dependence of structural integrity on the
204 dimensional features including the radius and thickness of the carbon coating and the
205 radius of the Si core. A design guideline for ensuring the structural integrity of
206 Si@void@C NPs is proposed which, in combination with the consideration of the
207 capacity as a function of these dimensional features, provides the direction for
208 maximizing the capacity of Si@void@C NPs. Optimized NPs are fabricated and found to
209 have improved capacity in comparison to the unoptimized ones. The results in this paper
210 should be of great value to the design of yolk-shell structured anode materials for lithium
211 ion battery with high capacity and excellent cycling performance.

212 **Acknowledgements**

213 This work was supported by the General Research Fund from Hong Kong RGC
214 (15206415, 529313). LZ acknowledges the financial support from the Hong Kong

215 Polytechnic University (Grant No. G-YBLF). HW would like to acknowledge the support
216 from the National Natural Science Foundation of China (11322219, 11321202).

217 **References**

- 218 [1] J.-M. Tarascon, M. Armand, Issues and challenges facing rechargeable lithium
219 batteries, *Nature* 414 (2001) 359-367.
- 220 [2] M. Endo, C. Kim, K. Nishimura, T. Fujino, K. Miyashita, Recent development of
221 carbon materials for Li ion batteries, *Carbon* 38 (2000) 183-197.
- 222 [3] Y. P. Wu, E. Rahm, R. Holze, Carbon anode materials for lithium ion batteries, *J.*
223 *Power Sources* 114 (2003) 228-236.
- 224 [4] M. T. McDowell, S. W. Lee, W. D. Nix, Y. Cui, 25th anniversary article:
225 understanding the lithiation of silicon and other alloying anodes for lithium-ion batteries,
226 *Adv. Mater.* 25 (2013) 4966-4985.
- 227 [5] C. K. Chan, H. Peng, G. Liu, K. McIlwrath, X. F. Zhang, R. A. Huggins, Y. Cui,
228 High-performance lithium battery anodes using silicon nanowires, *Nat. Nanotechnol.* 3
229 (2008) 31-35.
- 230 [6] H. Wu, G. Chan, J. W. Choi, I. Ryu, Y. Yao, M. T. McDowell, S. W. Lee, A.
231 Jackson, Y. Yang, L. Hu, Y. Cui, Stable cycling of double-walled silicon nanotube
232 battery anodes through solid-electrolyte interphase control, *Nat. Nanotechnol.* 7 (2012)
233 310-315.
- 234 [7] X. H. Liu, L. Zhong, S. Huang, S. X. Mao, T. Zhu, J. Y. Huang, Size-dependent
235 fracture of silicon nanoparticles during lithiation, *ACS Nano* 6 (2012) 1522-1531.
- 236 [8] H. Kim, J. Cho, Superior lithium electroactive mesoporous Si@carbon core-shell
237 nanowires for lithium battery anode material, *Nano Lett.* 8 (2008) 3688-3691.
- 238 [9] R. Huang, X. Fan, W. Shen, J. Zhu, Carbon-coated silicon nanowire array films
239 for high-performance lithium-ion battery anodes, *Appl. Phys. Lett.* 95 (2009) 133119.
- 240 [10] M. Zhou, T. Cai, F. Pu, H. Chen, Z. Wang, H. Zhang, S. Guan, Graphene/carbon-
241 coated Si nanoparticle hybrids as high-performance anode materials for Li-ion batteries,
242 *ACS Appl. Mater. Interfaces* 5 (2013) 3449-3455.
- 243 [11] Q. Li, W. Li, Q. Feng, P. Wang, M. Mao, J. Liu, L. Zhou, H. Wang, H. Yao,
244 Thickness-dependent fracture of amorphous carbon coating on SnO₂ nanowire electrodes,
245 *Carbon* 80 (2014) 793-798.
- 246 [12] W. Li, K. Cao, H. Wang, J. Liu, L. Zhou, H. Yao, Carbon coating may expedite
247 the fracture of carbon-coated silicon core-shell nanoparticles during lithiation, *Nanoscale*
248 8 (2016) 5254-5259.
- 249 [13] N. Liu, H. Wu, M. T. McDowell, Y. Yao, C. Wang, Y. Cui, A yolk-shell design
250 for stabilized and scalable Li-ion battery alloy anodes, *Nano Lett.* 12 (2012) 3315-3321.
- 251 [14] J. Yang, Y.-X. Wang, S.-L. Chou, R. Zhang, Y. Xu, J. Fan, W.-X. Zhang, H. K.
252 Liu, D. Zhao, S. X. Dou, Yolk-shell silicon-mesoporous carbon anode with compact solid
253 electrolyte interphase film for superior lithium-ion batteries, *Nano Energy* 18 (2015) 133-
254 142.

255 [15] X.-Y. Zhou, J.-J. Tang, J. Yang, J. Xie, L.-L. Ma, Silicon@carbon hollow core-
256 shell heterostructures novel anode materials for lithium ion batteries, *Electrochim. Acta*
257 87 (2013) 663-668.

258 [16] L. Su, J. Xie, Y. Xu, L. Wang, Y. Wang, M. Ren, Preparation and lithium storage
259 performance of yolk-shell Si@void@C nanocomposites, *Phys. Chem. Chem. Phys.* 17
260 (2015) 17562-17565.

261 [17] X. Li, P. Meduri, X. Chen, W. Qi, M. H. Engelhard, W. Xu, F. Ding, J. Xiao, W.
262 Wang, C. Wang, J.-G. Zhang, J. Liu, Hollow core-shell structured porous Si-C
263 nanocomposites for Li-ion battery anodes, *J. Mater. Chem.* 22 (2012) 11014-11017.

264 [18] S. Chen, M. L. Gordin, R. Yi, G. Howlett, H. Sohn, D. Wang, Silicon core-hollow
265 carbon shell nanocomposites with tunable buffer voids for high capacity anodes of
266 lithium-ion batteries, *Phys. Chem. Chem. Phys.* 14 (2012) 12741-12745.

267 [19] H. Tao, L.-Z. Fan, W.-L. Song, M. Wu, X. He, X. Qu, Hollow core-shell
268 structured Si/C nanocomposites as high-performance anode materials for lithium-ion
269 batteries, *Nanoscale* 6 (2014) 3138-3142.

270 [20] Y. Ru, D. G. Evans, H. Zhu, W. Yang, Facile fabrication of yolk-shell structured
271 porous Si-C microspheres as effective anode materials for Li-ion batteries, *RSC Adv.* 4
272 (2014) 71-75.

273 [21] W. Stöber, A. Fink, E. Bohn, Controlled growth of monodisperse silica spheres in
274 the micron size range, *J. Colloid Interface Sci.* 26 (1968) 62-69.

275 [22] X. Fang, S. Liu, J. Zang, C. Xu, M.-S. Zheng, Q.-F. Dong, D. Sun, N. Zheng,
276 Precisely controlled resorcinol-formaldehyde resin coating for fabricating core-shell,
277 hollow, and yolk-shell carbon nanostructures, *Nanoscale* 5 (2013) 6908-6916.

278 [23] S. P. Timoshenko, J. N. Goodier, *Theory of Elasticity*, third ed., McGraw-Hill
279 Book Co., Singapore, 1970.

280 [24] W.-J. Zhang, A review of the electrochemical performance of alloy anodes for
281 lithium-ion batteries, *J. Power Sources* 196 (2011) 13-24.

282 [25] A. Kushima, J. Y. Huang, J. Li, Quantitative fracture strength and plasticity
283 measurements of lithiated silicon nanowires by *in situ* TEM tensile experiments, *ACS*
284 *Nano* 6 (2012) 9425-9432.

285 [26] V. B. Shenoy, P. Johari, Y. Qi, Elastic softening of amorphous and crystalline Li-
286 Si phases with increasing Li concentration: a first-principles study, *J. Power Sources* 195
287 (2010) 6825-6830.

288 [27] M. G. Fyta, I. N. Remediakis, P. C. Kelires, D. A. Papaconstantopoulos, Insights
289 into the fracture mechanisms and strength of amorphous and nanocomposite carbon, *Phys.*
290 *Rev. Lett.* 96 (2006) 185503.

291 [28] M. A. Meyers, K. K. Chawla, *Mechanical Behavior of Materials*, second ed.,
292 Cambridge University Press, New York, 2009.

293 [29] Y. Huang, R. J. Young, Effect of fibre microstructure upon the modulus of PAN-
294 and pitch-based carbon fibres, *Carbon* 33 (1995) 97-107.

295 [30] C. K. Chan, X. F. Zhang, Y. Cui, High capacity Li ion battery anodes using Ge
296 nanowires, *Nano Lett.* 8 (2008) 307-309.

297 [31] J. R. Szczech, S. Jin, Nanostructured silicon for high capacity lithium battery
298 anodes, *Energy Environ. Sci.* 4 (2011) 56-72.

299